



Structural, optical, and electrical properties of $\text{Ni}_x\text{Zn}_{1-x}\text{Fe}_2\text{O}_4$ thin film prepared by spray pyrolysis route

Nawshin Yeasmin¹, M. K. R. Khan^{1,*}, M. M. Rahman¹, and M. S. I. Sarker^{1,*}

¹Department of Physics, University of Rajshahi, Rajshahi 6205, Bangladesh

Received: 7 March 2022

Accepted: 26 August 2022

Published online:

10 September 2022

© The Author(s), under exclusive licence to Springer Science+Business Media, LLC, part of Springer Nature 2022

ABSTRACT

Nanocrystalline spinel $\text{Ni}_x\text{Zn}_{1-x}\text{Fe}_2\text{O}_4$ ($x = 0.0, 0.3, 0.5, 0.7$) thin films have been deposited on glass substrate at temperature 350 °C via spray pyrolysis from metal nitrate aqueous solution. The thickness of the films ranges from 191 to 203 nm, whereas the average crystallite size ranges from 40 to 37 nm. The X-ray diffraction patterns confirm that the samples are well crystallized in the face-centered cubic spinel structure. Using cation distribution, the variation of theoretical and experimental lattice constant with Ni content is shown explicitly. The results of the optical measurement suggest that the Ni–Zn ferrite thin films are of direct band gap semiconductor and band gap energy varies from 2.50 to 2.23 eV. The Photoluminescence (PL) spectra of Ni–Zn ferrite thin films show that the emissions are due to the defect state transitions. The electrical resistivity for Ni–Zn ferrite thin films was measured as a function of temperature. The Hall constant, mobility, and carrier concentration of Ni–Zn ferrite thin films were calculated from the Hall effect study. It is found that the Ni–Zn ferrites are n-type semiconductor for $x = 0.0, 0.3, 0.5$ and starts to enter into p-type domain for $x = 0.7$.

1 Introduction

Spinel and garnet ferrites received considerable research interest having their possible potential applications in the field of science and technology including microwave application. For example, the ferrite thin films can be used in future radar and communication systems, transformers core, wastewater treatment, ferro-fluids, catalysts, etc. [1–7]. The

spinel ferrites have been manufactured in the form of nanostructured thick and thin films since 1990s [8]. Nevertheless, compared to other spinel ferrites, zinc ferrites (ZnFe_2O_4) have gained special focus due to the use of semiconductor photo catalyst with band gap 1.9 eV [9]. ZnFe_2O_4 is an important class of oxides having general formula AB_2O_4 , that contains two sub lattices named tetrahedral site and octahedral site in which Zn^{2+} ions occupied in the A-site and Fe^{3+}

Address correspondence to E-mail: mfkrKhan@yahoo.com; samiul-phy@ru.ac.bd

ions in the B-sites [10]. The cation distribution of these two sites strongly affects the electrical and magnetic properties of ferrite [11–14]. Among the various ferrites, Ni–Zn ferrites can be used generally for both high- and low-frequency devices as they have mechanical hardness, high Curie temperature, and low dielectric losses. Now in the modern technology, the bulk Ni–Zn ferrite components is incompatible with the fast growth of electronic applications which requires downsizing, lightweight, and multifunctional flexibility. To resolve complications in carrying out the desired miniaturization for devices, focus has been mostly paid on Ni–Zn ferrite films. The present investigation on Ni–Zn ferrite has focused to fabricate nanosized ferrite particles to diminish energy losses. It is necessary to attain ferrite materials in thin film form to easily integrate them into electronics devices [15]. In this context, study of structural, electrical, and optical properties of the materials is important. Moreover, in practice, materials that exhibit optical properties have special importance for applications directly linked with optic devices as filters, modulators, and switches. Hence, the research on Ni–Zn ferrite thin films is of special significance for their prospective implementation to sensor and on-chip integrated devices.

Ferrite nanomaterial can be produced through various methods such as citrate-route [16] wet chemical method [17], spin-coating method [18], mechanical alloying method [19], combustion method, etc. [20]. Spray pyrolysis holds different types of benefits such as excellent control of chemical uniformity, high purity, and stoichiometry of multi-component system compared to other chemical deposition methods [21]. The other favor of the spray pyrolysis method is that it can be accommodated without difficulty for generation of large-area films [22]. Currently, some research on Ni–Zn ferrite nanoparticles has been performed including synthesis of nanosized nickel zinc ferrite using electric arc furnace dust and ferrous pickle liquor [23], structural and magnetic properties of Ni–Zn ferrite nanoparticles synthesized by a thermal decomposition method [24], effect of Ni–Zn ferrite nanoparticles upon the structure, magnetic, and gyromagnetic properties of low-temperature processed LiZnTi ferrite [25]. The improved saturation magnetization and initial permeability in Mn–NiZn ferrites after cooling in vacuum have also been reported [26]. In addition, a few works on microstructural, magnetic, and optical

properties of Ni–Zn ferrites via spray pyrolysis have been focused [27, 28]. However, it is also crucial to study electric properties of the Ni–Zn ferrites along with other surface and physical properties considering practical demands. Therefore, the purpose of the current work is to set nanocrystalline $\text{Ni}_x\text{Zn}_{1-x}\text{Fe}_2\text{O}_4$ thin films on glass substrates through spray pyrolysis and to study their structural, optical, dielectric, and electrical properties in details.

2 Experimental details

The preparation of experimental samples of $\text{Ni}_x\text{Zn}_{1-x}\text{Fe}_2\text{O}_4$ ($x = 0.0, 0.3, 0.5, 0.7$) was carried out by a conventional spray pyrolysis method. The appropriate volumes of 0.1 M Zinc nitrate hexahydrate [$\text{Zn}(\text{NO}_3)_2 \cdot 6\text{H}_2\text{O}$ (98%, LOBA Chemie)], 0.1 M Iron nitrate nonahydrate [$\text{Fe}(\text{NO}_3)_3 \cdot 9\text{H}_2\text{O}$ (98% Merck)], and 0.1 M Nickel nitrate hexahydrate [$\text{Ni}(\text{NO}_3)_2 \cdot 6\text{H}_2\text{O}$, 99.9% pure, ALDRICH] were mixed in distilled water. In a container, 90 ml of pre-cursor solution is taken and fitted up through the spray nozzle. The clean substrate with a suitable mask was put on the susceptor of the heater. The separation between the surface of the substrate and tip of the nozzle was 23 cm. By regulating the heater power using a variac, the substrate temperature was controlled at 350 °C. The solution flow rate was 0.5 ml/min and sprayed continuously for 40 min to produce $\text{Ni}_x\text{Zn}_{1-x}\text{Fe}_2\text{O}_4$ thin films. All these parameters were kept constant for obtaining film of same thickness of all concentrations as we are not interested to thickness-dependent physical properties.

The thickness of the deposited films was evaluated using the Newton's ring method (its working principle is interference and based on the fact that the formation of bright and dark interference fringes which is actually the measure of the thickness of air film at that point) and estimated to 200 ± 10 nm and the crystal structure is characterized by X-Ray diffraction (XRD) analysis using (Bruker D2 Phaser XRD machine, Hongkong) with CuK_α radiation, FTIR analysis by a spectrophotometer (Perkin Elmer 100), The SEM images and EDX analysis were performed by Field emission scanning electron microscopy (FE-SEM, JEOL JSM-7600 F), optical measurement by (SHIMADZU UV-1650PC spectrophotometer), photoluminescence (RTPL) spectra using spectrofluorophotometer (Hitachi F-4600), Electrical and

Hall measurement by Van-der Pauw's method [29, 30].

3 Results and discussion

3.1 Structural properties

3.1.1 XRD analysis

Figure 1a shows a typical XRD pattern of Ni–Zn ferrite thin films. The multiple peaks were identified as (2 2 0), (3 1 1), (2 2 2), (4 0 0), (5 1 1), and (4 4 0), which confirm that Ni–Zn ferrite is well crystallized in face-centered cubic structure (JCPDS card no. (#08-0234)) with $Fd\bar{3}m$ space group [31, 32]. In all cases, the most intense reflection is noticed from the (3 1 1)

plane indicating the spinel phase formation. It is also observed that initially the diffraction peaks shift toward the left due to lattice distortion and then toward the right with the increase of Ni concentration as is evidenced in Fig. 1b.

The values of lattice constant, a , are evaluated from the XRD data for all the specimens. The average lattice constants (taking all planes into consideration) for cubic crystal system of the synthesized thin films are calculated through $a = d_{hkl} \sqrt{h^2 + k^2 + l^2}$, where d_{hkl} is the interplanar spacing and (h k l) are the Miller indices of the diffraction peak [33]. The calculated average lattice constant, a , as a function of Ni content is plotted in Fig. 2. It is seen from Fig. 2a that the lattice constants decrease almost linearly from 8.334 to 8.299 Å with increasing Ni^{2+} concentrations

Fig. 1 **a** XRD pattern of $Ni_xZn_{1-x}Fe_2O_4$ thin films **b** shifting of intense peak (311)

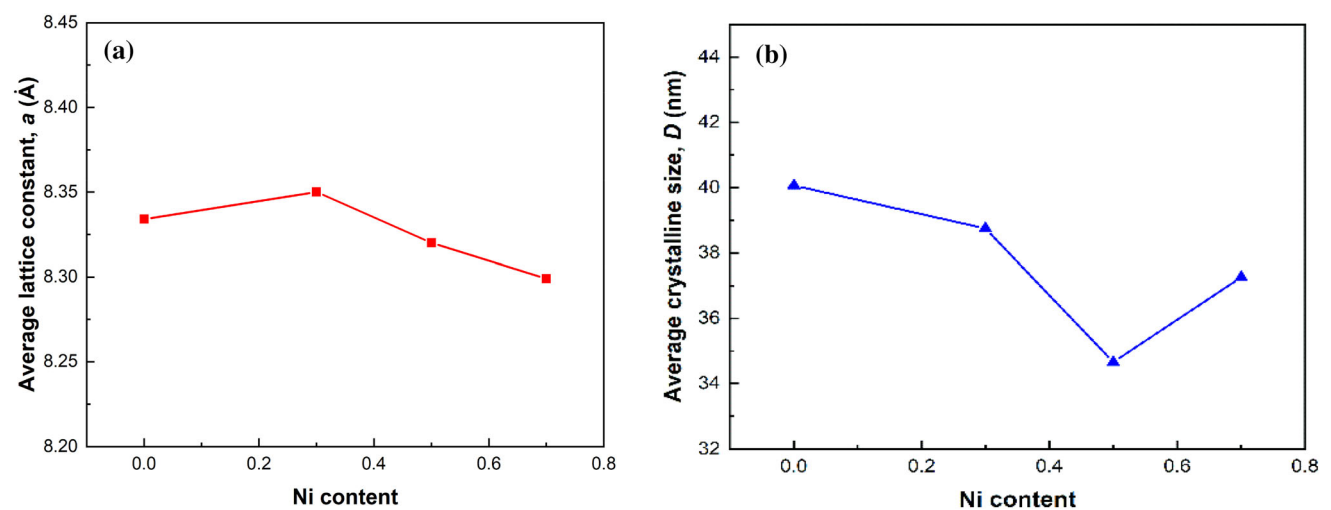
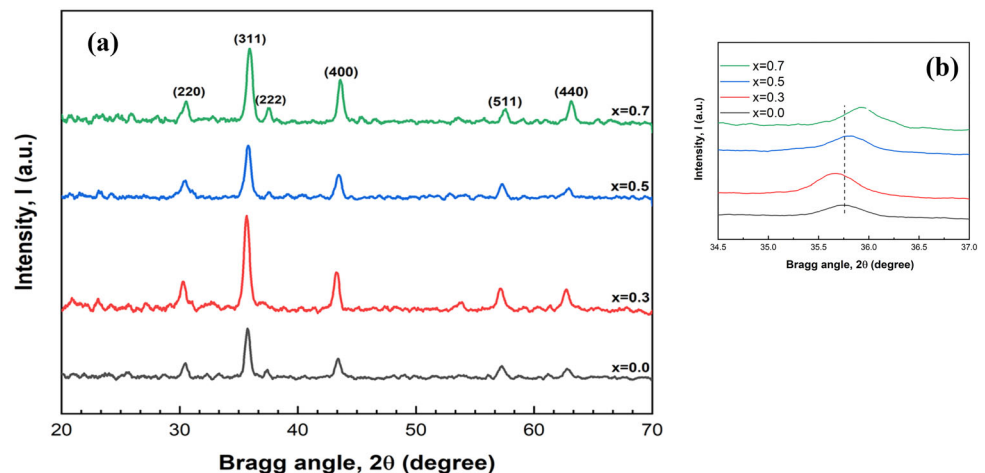


Fig. 2 Variation of **a** lattice constant and **b** crystallite size with Ni content

except for $x = 0.3$. [34]. From Fig. 2a, it is seen that the lattice constant at first increases for $x = 0.3$ and then decreases. This increase of lattice constant is due to the redistribution of cations in octahedral (A) and tetrahedral (B) sites [35]. Another possible reason is the creation of Fe vacancies during crystal formation, resulting in the increase of lattice constant. However, the reduction in lattice constant after $x = 0.3$ is certainly a result of substitution of larger Zn^{2+} (0.74 Å) ions by smaller Ni^{2+} ions (0.69 Å). The crystallite size, D of $Ni_xZn_{1-x}Fe_2O_4$ ferrite thin films is estimated by using Debye Scherrer’s formula [36], $D = \frac{k\lambda}{\beta\cos\theta}$, where k is a constant (0.94), $\lambda = 1.540 \text{ \AA}$ is the x-ray radiation wavelength, β is the full width at half maximum (FWHM), and θ is the diffraction angle.

The calculated average crystallite size, D , as a function of Ni content is plotted in Fig. 2b. The crystallite size varies between 40 and 37 nm with Ni concentration. From Fig. 2b, it is seen that the average crystallite size decreases with the increase of Ni^{2+} content, but increases for 0.7 Ni content. The crystallite size usually depends on thermodynamics and

especially on the growth parameters including substrate temperature, solution concentration, spray rate, etc. Since all these parameters are not equally controllable simultaneously, hence the fluctuation of crystal size is not unlikely.

The hopping length L_A in the A-site (tetrahedral) and L_B in the B-site (octahedral) can be calculated by using the relations $L_A = 0.25a\sqrt{3}$ and $L_B = 0.25a\sqrt{3}$ where a is the calculated lattice constant. Figure 3 depicts the hopping lengths in tetrahedral and octahedral sites with Ni content, respectively. The decrease of hopping length in both tetrahedral and octahedral sites (the shortened of the separation of magnetic ions) is noticed with the increase of Ni^{2+} content except for $x = 0.3$ [37]. This is due to the smaller radius (0.69 Å) of Ni^{2+} ion than Zn^{2+} ion (0.74 Å). Hopping length in A-site decreases from 3.6088 to 3.5934 Å and in B-site from 2.9466 to 2.9340 Å. The hopping length at A-site is comparatively larger than the value of B-site. This may be due to the fact that, the distance between the magnetic ions in tetrahedral site is greater than the octahedral site.

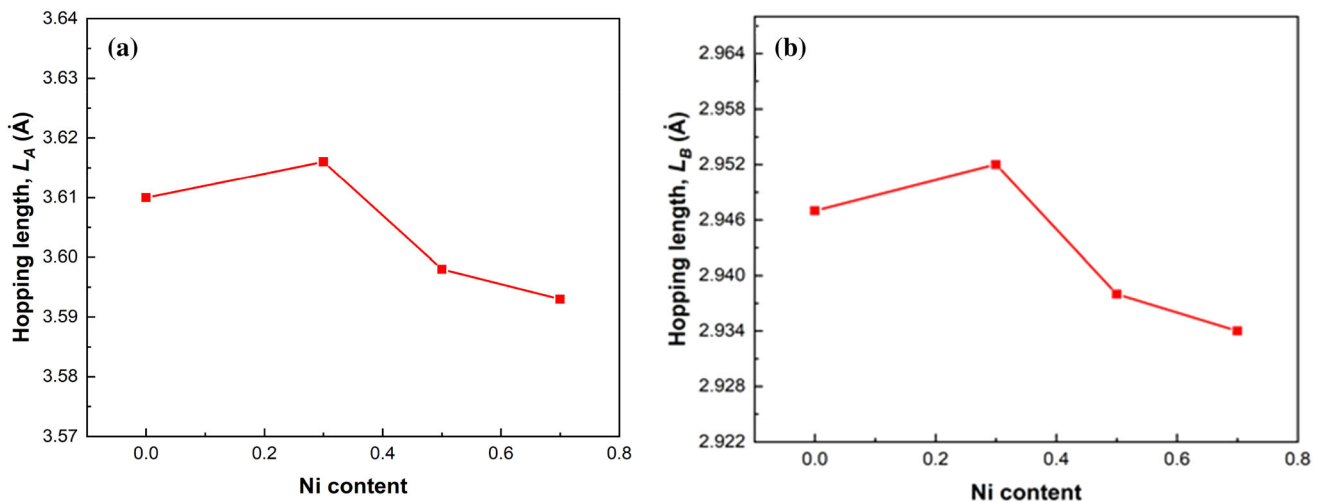


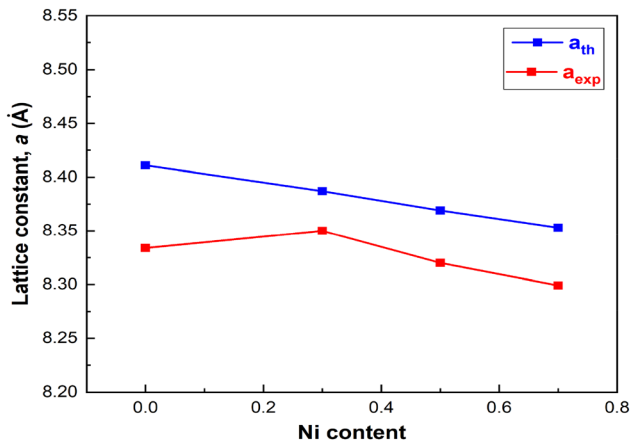
Fig. 3 Variation of hopping length in a A-site and b B-site with Ni content

Table 1 Calculated lattice volume, molecular weight, X-ray density, and interatomic distance between the cations

Ni content, x	Volume, V (Å ³)	Molecular weight, M (gm/mol)	X-ray density, ρ_x (gm/cm ³)	$M_B - M_A$ (Å)	$M_A - M_B$ (Å)	$M_B - M_B$ (Å)
0.0	578.84	241.097	5.53	3.608	3.455	2.946
0.3	582.18	239.082	5.45	3.616	3.463	2.952
0.5	575.93	237.739	5.48	3.598	3.445	2.937
0.7	571.58	236.396	5.49	3.593	3.440	2.934

Table 2 Chemical formula, cation distribution, theoretical (a_{th}), and experimental (a_{expt}) lattice parameters

Ni content, x	Chemical formula	Cation distribution	r_A (Å)	r_B (Å)	a_{th} (Å)	a_{exp} (Å)
0.0	ZnFe ₂ O ₄	(Zn _{1.0}) _A [Fe _{2.0}] _B	0.740	0.645	8.411	8.334
0.3	Ni _{0.3} Zn _{0.7} Fe ₂ O ₄	(Zn _{0.7} Fe _{0.3}) _A [Ni _{0.3} Fe _{1.7}] _B	0.712	0.652	8.387	8.350
0.5	Ni _{0.5} Zn _{0.5} Fe ₂ O ₄	(Zn _{0.5} Fe _{0.5}) _A [Ni _{0.5} Fe _{1.5}] _B	0.693	0.656	8.369	8.320
0.7	Ni _{0.7} Zn _{0.3} Fe ₂ O ₄	(Zn _{0.3} Fe _{0.7}) _A [Ni _{0.7} Fe _{1.3}] _B	0.674	0.661	8.353	8.299

**Fig. 4** Variation of theoretical and experimental lattice constant with Ni content

The interatomic distance between the cations on the tetrahedral (A) and octahedral (B) sites can be computed using [38] $M_A - M_A = \frac{\sqrt{3}}{4}a$, $M_A - M_B = \frac{\sqrt{11}}{8}a$, $M_B - M_B = \frac{\sqrt{2}}{4}a$. The lattice volume, molecular weight, x-ray density, and interatomic distance between the cations are tabulated in Table 1.

Lattice constants can also be calculated theoretically from the following equation $a_{th} = \frac{8}{3\sqrt{3}}[(r_A + R_O) + \sqrt{3}(r_B + R_O)]$, where R_O is the radius of oxygen ion and r_A , r_B are the ionic radius for tetrahedral (A) and octahedral (B) sites of spinel structure, respectively [39].

The r_A and r_B values are calculated using the cationic distribution of the cubic spinel system which can be represented by the following equation [40] $r_A = C_{AFe}r(Fe^{3+}) + C_{AZn}r(Zn^{2+})$, $r_B = \frac{1}{2}[C_{BFe}r(Fe^{3+}) + C_{BNi}r(Ni^{2+})]$. The ionic radii for Zn, Fe, and Ni are 0.74, 0.645, and 0.69 Å, respectively. The Chemical formula, cation distribution, theoretical (a_{th}), and experimental (a_{expt}) lattice parameters are tabulated in Table 2.

The cation distribution of Ni–Zn ferrite is mixed spinel type having the formula $(Zn_{1-x}Fe_x)_A$

$[Ni_x^{2+}Fe_{2-x}^{3+}]_B O_4^{2-}$, where A and B mean the tetrahedral and octahedral sites, respectively. Due to the favorable fit of charge distribution of Ni^{2+} ions in the crystal field of the octahedral site, they exhibit a propensity to go into the B-sites in the crystal lattice. On other hand, Zn^{2+} ions prefer to go to the A-site for their affinity to form covalent bonds involving sp^3 hybrid orbitals [41]. The variation of theoretical and experimental lattice constants with Ni content is as shown in Fig. 4.

From Fig. 4, it is observed that the experimental lattice constant does not follow entirely with the theoretical lattice constant. The theoretical lattice parameter decreases with Ni content but in experimental case lattice parameter first increases and then decreases with increasing Ni content. The experimental lattice constant fluctuation is due to the defects and thermal effects.

3.1.2 SEM study

Scanning electron microscopy was performed to study the surface morphology of prepared Ni–Zn ferrite thin films. The SEM image of $Ni_xZn_{1-x}Fe_2O_4$ of various concentrations ($x = 0.0, 0.3, 0.5, 0.7$) is given in Fig. 5. SEM micrographs clearly show the distribution of spherical grains of uneven size and density over the film surface.

3.1.3 Elemental analysis

Figure 6 reveals the EDX investigations of the $Ni_xZn_{1-x}Fe_2O_4$ thin films for $x = 0.0$ to 0.7 concentrations. The presence of Zn, Fe, O, and Ni compositions in the zinc ferrite samples is confirmed by the EDX study. The qualitative data of the compositions are compared with the theoretical value, which is tabulated in Table 3.

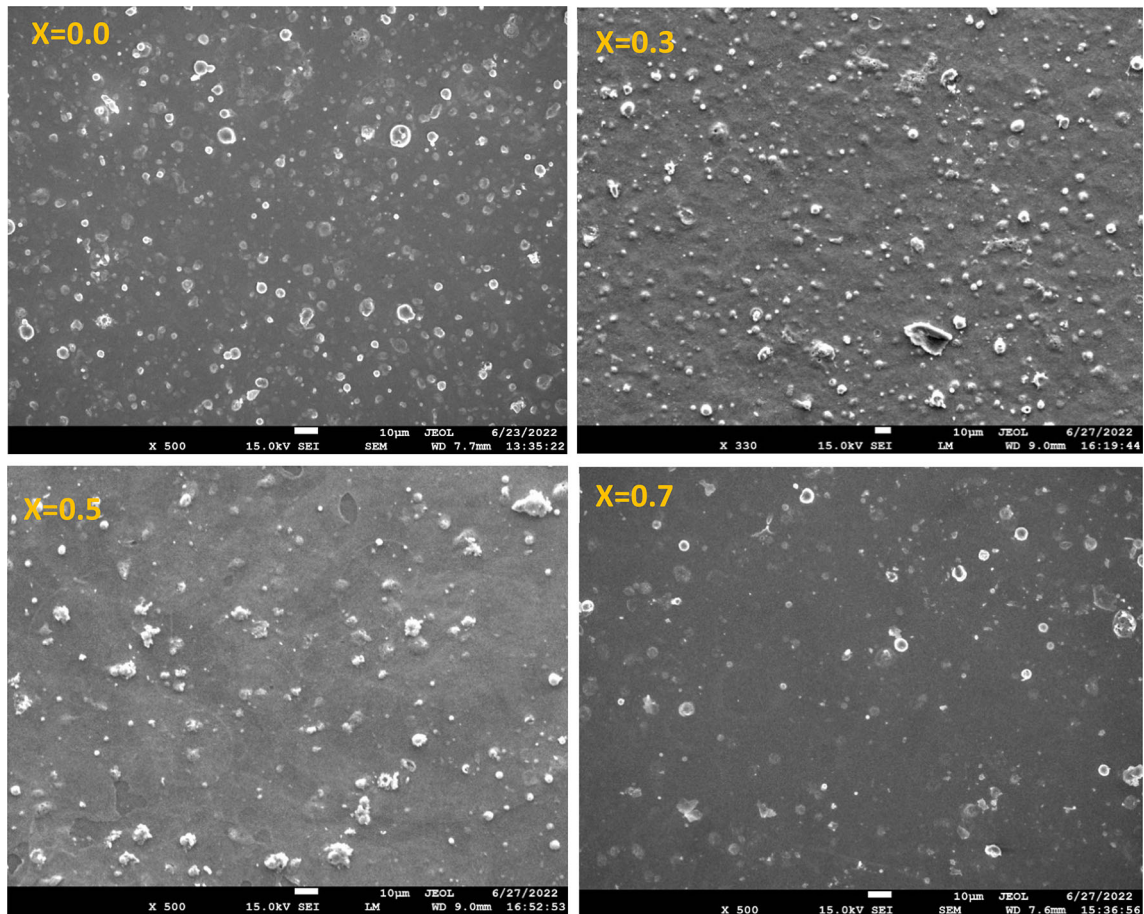


Fig. 5 SEM image of $\text{Ni}_x\text{Zn}_{1-x}\text{Fe}_2\text{O}_4$ thin films for various concentration of Ni ions

3.1.4 FTIR study

Figure 7 shows the FTIR spectrum of $\text{Ni}_x\text{Zn}_{1-x}\text{Fe}_2\text{O}_4$ thin films in the wave number range from 250 to 4000 cm^{-1} . The absorption peak at 3432 cm^{-1} is occurred due to the O-H bending vibrations indicating the presence of moisture in the sample. The observed peak 2340.65 cm^{-1} is assigned to C-H bending vibrations. These O-H and C-H bending vibrations are attributed due to the absorption of water and atmospheric carbon dioxide by the sample during sample preparation process. Furthermore, with increasing Ni concentrations the peaks are shifted to the higher wavenumber indicating changes in the bond angle due to the replacement of Zn by Ni ions.

3.1.5 Optical study

Optical properties of the films are also examined thoroughly. Figure 8a shows the variation of

$\text{Ni}_x\text{Zn}_{1-x}\text{Fe}_2\text{O}_4$ thin films transmittance $T(\lambda)$ with incident photon wavelength (λ) for $\text{Ni}_x\text{Zn}_{1-x}\text{Fe}_2\text{O}_4$ thin films. It shows the transmittance rapidly increases with the increase of wavelength in the range of (380–680) nm and then it increases slowly in all cases. Besides, the transmittance decreases with the increase of Ni concentration and varies on an average from 62 to 50%. In Fig. 8a, if we take a close look, a very faint absorption hump is observed also for $x = 0.7$ sample around at 750 nm indicated by an arrow. It is assumed that the d-d transition in Fe^{3+} ion in an octahedral symmetry is responsible for this. For spinel ferrites, the observed optical absorption bands are assumed to d-d intra-atomic transitions in the Fe^{3+} cations and interatomic $\text{Fe}^{3+}-\text{O}_2$ transitions between oxygen atomic 2p-orbitals and iron atomic 3d (t_{2g})-orbitals. In the UV region, zinc interatomic $\text{Zn}^{2+}-\text{O}^{2-}$ transitions occur forming Zn^{2+} ion with a completely full 3d sub-shell [42]. In similar with iron, the intra-atomic d-d transitions take place between

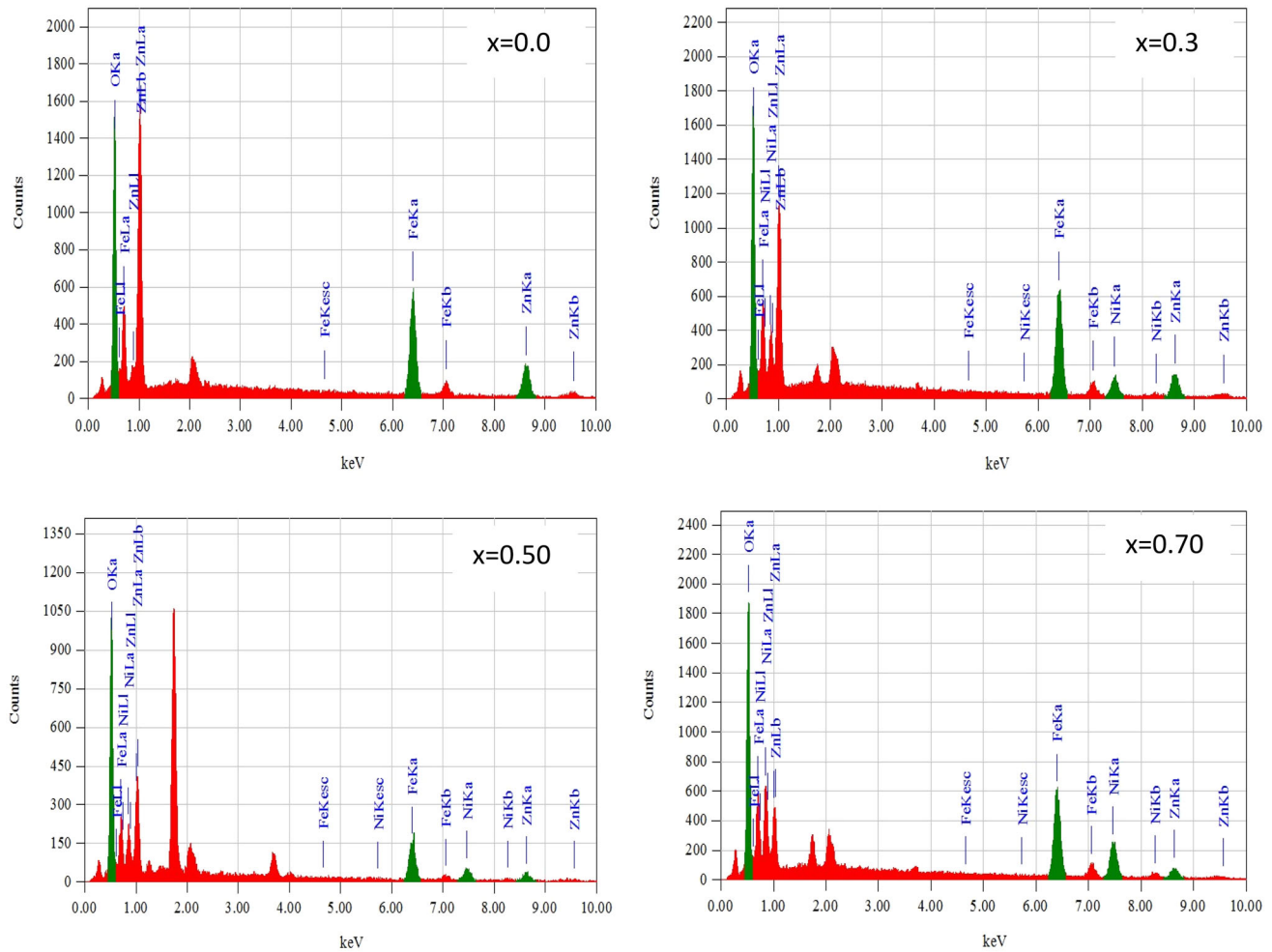


Fig. 6 EDX analysis of the as-synthesized $\text{Ni}_x\text{Zn}_{1-x}\text{Fe}_2\text{O}_4$ thin films for $x = 0.0, 0.3, 0.5,$ and 0.7 concentrations

Table 3 Atomic weight (%) of the as-synthesized $\text{Ni}_x\text{Zn}_{1-x}\text{Fe}_2\text{O}_4$ thin films for $x = 0.0$ to 0.7 concentrations

Element	$x = 0.0$		$x = 0.3$		$x = 0.5$		$x = 0.7$	
	Theoretical (wt%)	Experimental (wt%)	Theoretical (wt%)	Experimental (wt%)	Theoretical (wt%)	Experimental (wt%)	Theoretical (wt%)	Experimental (wt%)
Zn	27.12	39.09	19.15	26.52	13.75	17.41	8.30	12.61
Fe	46.33	38.85	46.72	39.68	46.98	30.11	47.25	36.52
O	26.54	22.06	26.76	21.95	26.91	36.81	27.07	23.19
Ni	-	-	7.37	11.85	12.35	15.67	17.38	27.68

different valence ions in the NIR region in case of nickel [43].

In the transmission curves, there is no significant sign of second transition. Therefore, the direct band gap was determined by Tauc's equation [44] $\alpha h\nu = A(h\nu - E_g)^n$, where α is the absorption coefficient, $h\nu$ is

the photon energy, A is the constant which does not depend on photon energy, and n has four numeric values. Figure 9a shows the direct band gap of Ni–Zn ferrite thin film decreases from 2.50 to 2.23 eV with the increase of Ni concentration consistent with [45].

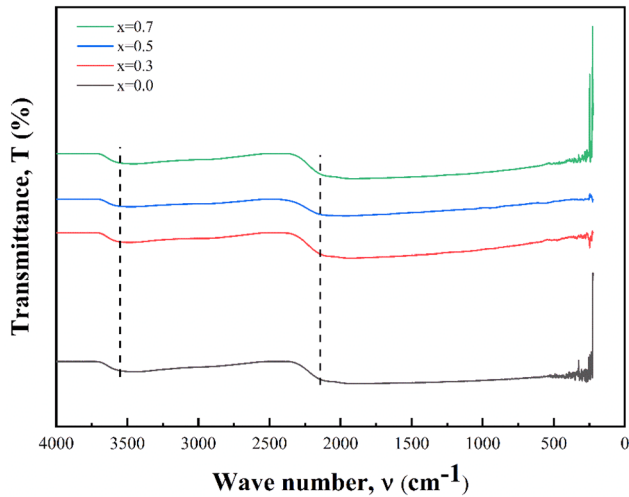


Fig. 7 FTIR spectra for $\text{Ni}_x\text{Zn}_{1-x}\text{Fe}_2\text{O}_4$ thin films for various concentrations of Ni content

Direct band gap energy in electron volt has been tabulated in Table 4.

The change of direct band gap with composition is shown in Fig. 9b where we can see that the band gap decreases with increasing Ni concentrations. The shrinkage of band gap is due to the structural modification of ZnFe_2O_4 films. Such structural modification in the ZnFe_2O_4 films is associated with the replacement of zinc ions both in lattice site and interstitial position in the ZnFe_2O_4 lattice by Ni ions [46, 47]. Although α depends on film thickness; however, it is assumed that the band gap energy variation is solely originated from the composition

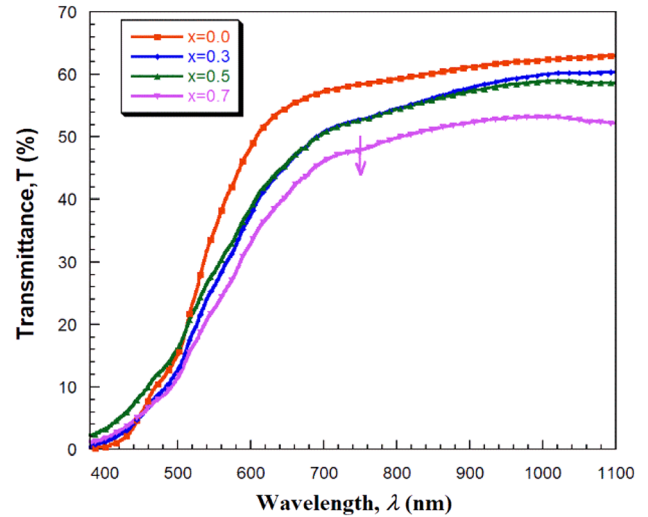


Fig. 8 Variation of transmittance with wavelength for different compositions

Table 4 The direct band gap of $\text{Ni}_x\text{Zn}_{1-x}\text{Fe}_2\text{O}_4$ thin films (average thickness 200 ± 10 nm) with different compositions

Composition, x	Direct band gap (eV)
0.0	2.50
0.3	2.40
0.5	2.32
0.7	2.23

because the variation of film thickness is so small to contribute the band gap.

The photoluminescence (PL) spectra of the $\text{Ni}_x\text{Zn}_{1-x}\text{Fe}_2\text{O}_4$ ($x = 0.0, 0.3, 0.5, 0.7$) thin films were

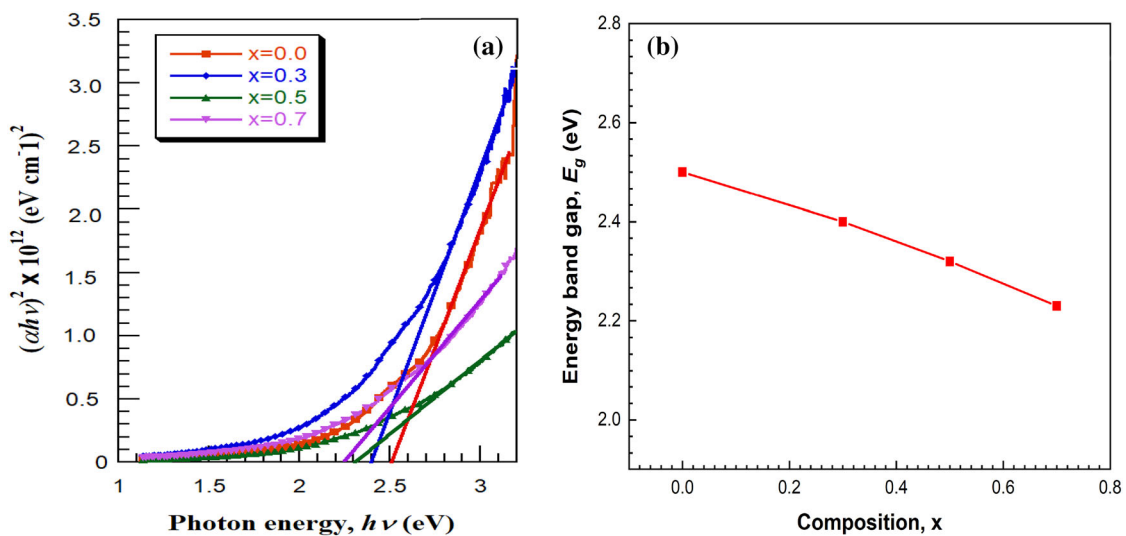


Fig. 9 Variation of **a** direct band gap with photon energy and **b** band gap with the composition of $\text{Ni}_x\text{Zn}_{1-x}\text{Fe}_2\text{O}_4$ thin films

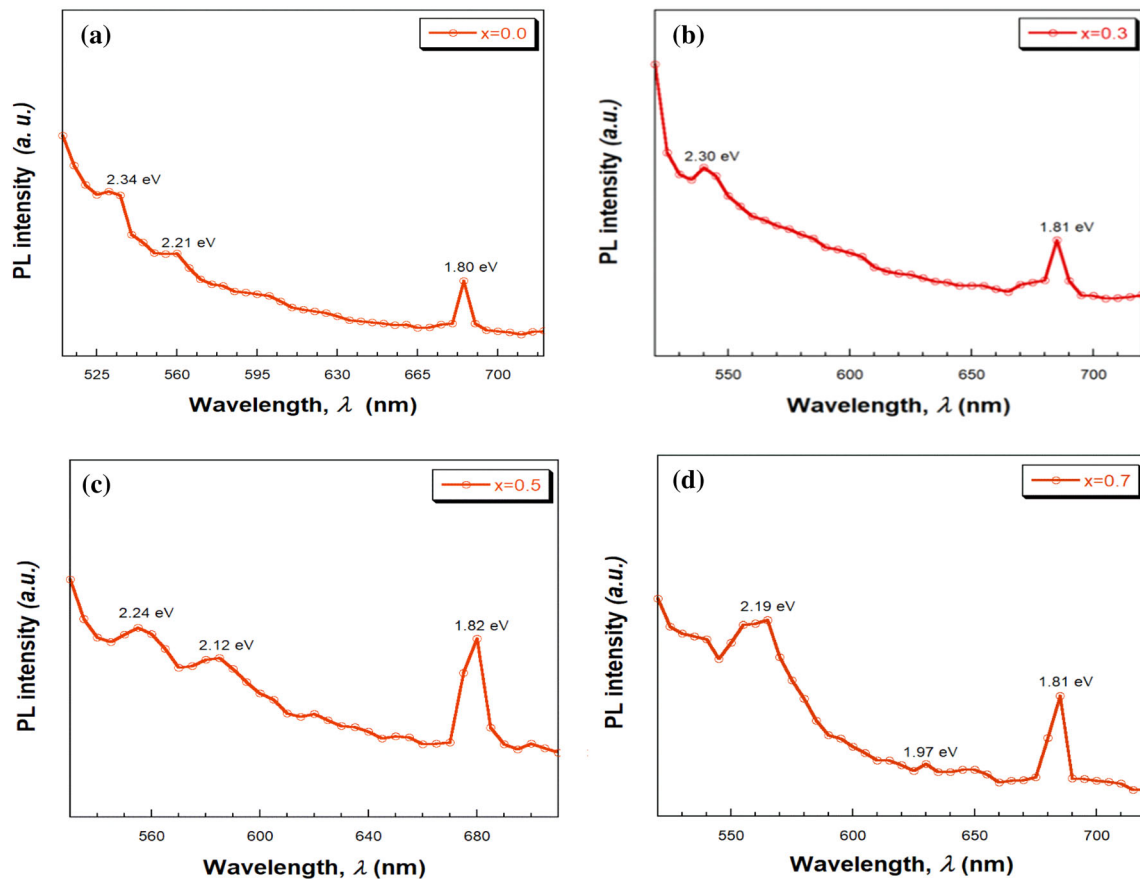


Fig. 10 PL spectra of $\text{Ni}_x\text{Zn}_{1-x}\text{Fe}_2\text{O}_4$ for different compositions of Ni **a** $x = 0.0$, **b** $x = 0.3$, **c** $x = 0.5$, and **d** $x = 0.7$

taken at room temperature with excitation wavelength, $\lambda_{ex} = 450$ nm (2.75 eV) as shown in Fig. 10. From PL study, it is observed that the emissions are found at 529.91 nm (2.02 eV), 561.09 nm (2.21 eV), and 688.89 nm (1.80 eV) for $x = 0.0$. For $x = 0.3$, the emissions are found at 539.13 nm (2.30 eV) and 685.08 nm (1.81 eV). For $x = 0.5$, the emissions are found at 553.57 nm (2.24 eV), 584.91 nm (2.12 eV), and 681.32 nm (1.82 eV). Furthermore, emissions are found at 566.21 nm (2.19 eV), 629.44 nm (1.97 eV), and 685.08 nm (1.81 eV) for $x = 0.7$. All these PL emission energies are lower than optical band gap energies indicating PL transitions are not from band to band rather coming from defect states and oxygen vacancies which were originated from substitution of Ni at Zn sites and interstitials. The defect states due to substitution act as PL centers and eventually PL transition occurs which attributed to the defect state transitions [48, 49].

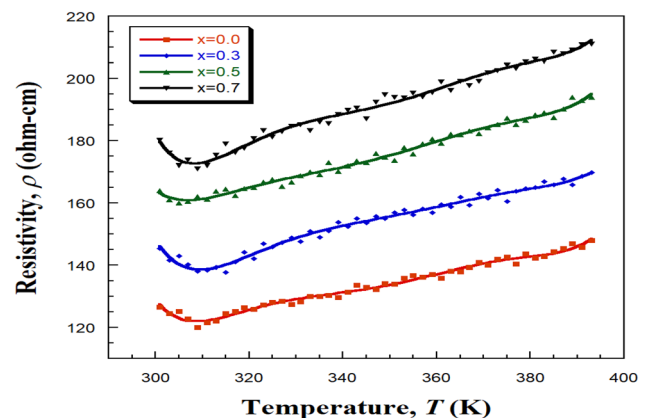


Fig. 11 Variation of resistivity with temperature for $\text{Ni}_x\text{Zn}_{1-x}\text{Fe}_2\text{O}_4$ thin films

3.1.6 Electrical study

The temperature-dependent resistivity for the films of $\text{Ni}_x\text{Zn}_{1-x}\text{Fe}_2\text{O}_4$ has been measured for the temperature range (290–400) K using Vander Pauw's method. Figure 11 shows the variation of resistivity and conductivity with temperature for

Table 5 Calculated data of Hall constant, Hall mobility, and carrier concentration for $\text{Ni}_x\text{Zn}_{1-x}\text{Fe}_2\text{O}_4$ thin films

Composition, x	Thickness t (nm)	Hall voltage, V_H (mV)	Hall constant, $R_H \times 10^6$ ($\text{cm}^3/\text{coul.}$)	Hall mobility, $\mu_H \times 10^2$ ($\text{cm}^2/\text{V}\cdot\text{sec}$)	Carrier concentration, $n \times 10^{13}$ (cm^{-3})	Resistivity ρ ($\Omega\text{-cm}$)
0.0	191	7.6	0.110	8.692	5.693	126.56
0.3	195	14.6	0.219	15.07	2.857	145.28
0.5	203	30.0	0.460	28.06	1.360	163.96
0.7	208	27.0	0.424	23.52	1.474	180.28

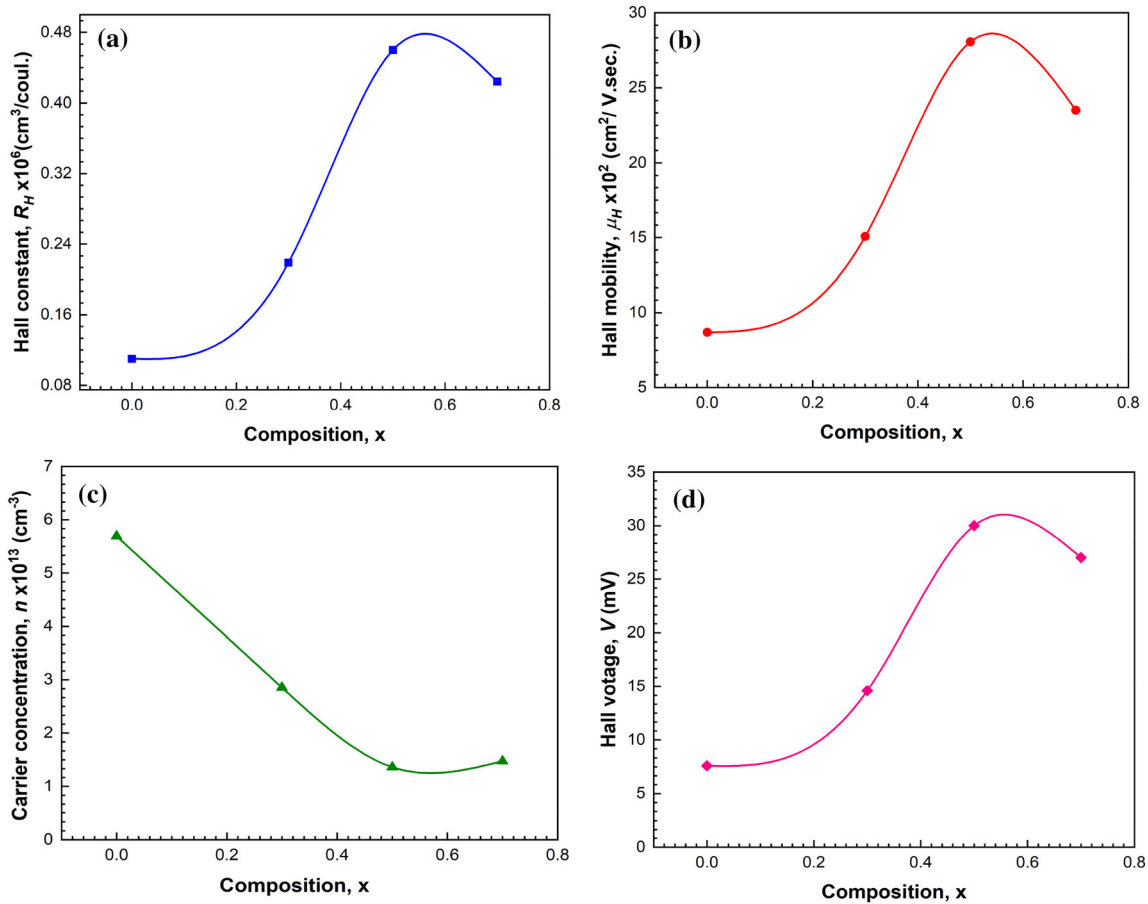


Fig. 12 Variation of **a** Hall constant, **b** Hall mobility, **c** Hall concentration, and **d** Hall voltage with composition for $\text{Ni}_x\text{Zn}_{1-x}\text{Fe}_2\text{O}_4$ thin films

$\text{Ni}_x\text{Zn}_{1-x}\text{Fe}_2\text{O}_4$ thin films, respectively. From Fig. 11, it is seen that the resistivity slightly decreases as the temperature increases which behaves like semiconductor material up to ~ 310 K. After 310 K, the electrical resistivity increases linearly with increasing temperature demonstrated metal-like behavior. Moreover, the resistivity increases with the increase

of Ni concentration. The resistivity of $\text{Ni}_x\text{Zn}_{1-x}\text{Fe}_2\text{O}_4$ compound should decrease with the doping of metallic Ni atom. However, it seems crystal lattice distortion and more and more oxygen vacancies due to progressing doping suppress the conductivity. This explanation supported by Hall study where we

find decreasing carrier concentration with increasing doping content.

At room temperature and constant magnetic field of 9.815 KG, the Hall voltage has been measured. From the Hall voltage, the Hall constant (R_H), Hall mobility (μ_H), and carrier concentration (n) are calculated (Table 5). In this work, Fig. 12a, b and d shows the Hall constant and Hall mobility increase with increasing Ni concentration except for $x = 0.7$. The carrier concentration decreases with Ni concentration, while for $x = 0.7$, it increases (Fig. 12c). From the Hall measurement, $Ni_xZn_{1-x}Fe_2O_4$ thin films are identified as n-type materials for $x = 0.0, 0.3, 0.5$ and p-type for $x = 0.7$. Generally, $NiFe_2O_4$ is known as p-type semiconductor with cation vacancies for its tendency to attract oxygen during heating [50, 51], whereas zinc ferrite is n-type semiconductor [52]. So according to the above information, it can be said that, for comparatively high concentration of Ni ($x = 0.7$), the n-type material has turned into p-type material.

4 Conclusions

We have demonstrated well-crystallized spinel $Ni_xZn_{1-x}Fe_2O_4$ thin films by spray pyrolysis deposition process and different characteristics studied as a function of Ni content. The lattice constants obtained from XRD data vary from 8.334 Å to 8.299 Å with Ni substitution. The decrease of lattice constant of these films with Ni content is attributed to the replacement of a larger Zn^{2+} ion (0.74 Å) by a smaller Ni^{2+} (0.69 Å) ion. SEM study of thin films reveals the formation of spherical grains distributed over the film surface with various densities depending on the Ni concentration. From optical study, we noticed that the band gap energy decreased from 2.50 to 2.23 eV with the increasing Ni concentration due to the formation of oxygen vacancy and defects. Electrical measurement demonstrates semiconductor behavior of Ni–Zn ferrite thin films up to 310 K followed by metal-like behavior up to the measured temperature range. Although Ni–Zn ferrite thin films show metal-like behavior, the resistivity is comparatively high and increased with the increasing of Ni concentration which is significant for high- and low-frequency device applications. The Hall measurement confirms that Ni–Zn ferrites change its semiconducting nature from n-type to p-type semiconductor at $x = 0.7$.

Acknowledgements

We gratefully acknowledge M Nurul Huda Liton for providing XRD data during his Ph.D program at Hong Kong and M Tanveer Karim, Lecturer, Dept. of Physics, RUET for providing us the Photoluminescence (PL) data.

Author contributions

NY: Methodology, investigation, writing—original draft, writing—review and editing. MKRK: Conceptualization, methodology, investigation, supervision, writing—review and editing. MMR: Resources, MSIS: Conceptualization, methodology, supervision, writing—original draft, writing—review and editing.

Data availability

The experimental data which support the findings of this study are available on request from the corresponding author.

Declarations

Conflict of interest The authors declare no competing financial interests.

References

1. J.L. Deschanvres, M. Langlet, J.C. Joubert, J. Magn. Mater. **83**, 437–438 (1990)
2. A. Shahsavari, R. Ansarian, M. Bahiraei, Powder Technol. **340**, 370–379 (2018)
3. S.Q. Liu, X.L. Zhu, Y. Zhou, Z.D. Meng, Z.G. Chen, C.B. Liu et al., Catal. Sci. Technol. **7**(15), 3210–3219 (2017)
4. V. Adimule, M.G. Revaigh, H J. Adarsh, J. Mater. Eng. **29**, 4586–4596 (2020)
5. V. Adimule, D. Bhowmik, A. Suryavanshi, IOP Conf. Ser. **577** 012032 (2019)
6. V. Adimule, S.S. Nandi, B.C. Yallur, D. Bhowmik, A.H. Jagadeesha, Mater. Today Chem. **20**, 100438 (2021)
7. V. Adimule, S.S. Nandi, B.C. Yallur et al., J. Fluoresc. **31**, 487–499 (2021)
8. A. Sutka, G. Strikis, G. Mezinskas, A. Lasis, J. Zavickis, J. Kleperis, D. Jakovlevs, Thin Solid Films **526**, 65–69 (2012)
9. R.K. Sharma, R. Ghose, Ceram. Int. **41**, 14684 (2015)

10. M. Atif, S. Hasanain, M. Nadeem, *Solid State Commun.* **138**(8), 416–421 (2006)
11. A. Hossain, M.S.I. Sarker, M.K.R. Khan, F.A. Khan, M. Kamruzzaman, M.M. Rahman, *Appl. Phys. A* **124**, 608 (2018)
12. A. Hossain, M.S.I. Sarker, M.K.R. Khan, M.M. Rahman, *Mater. Sci. Eng. B* **253**, 114496 (2020)
13. M.A.A. Mamun, M.S.I. Sarker, M.R. Hasan, M.M. Haque, F.A. Khan, M.M. Rahman, M.K.R. Khan, *Result Phys.* **29**, 104698 (2021)
14. A. Ali, M.S.I. Sarker, M. Islam, M.K.R. Khan, F.A. Khan, M.N.I. Khan, M.M. Rahman, *Result Phys.* **25**, 104251 (2021)
15. S.S. Kumbhar, M.A. Mahadik, V.S. Mohite, Y.M. .Hunge, K.Y. Rajpure, C.H. Bhosale, *Mater. Res. Bull.* **67**, 47–54 (2015)
16. N. Gupta, A. Verma, C. Subhash, D. Kashyap, C. Dube, *Solid State Commun.* **134**, 689–694 (2005)
17. Q. Tian, J. Gong, Q. Wang, S. Wang, X. Zhang, *Thin Solid Films* **518**, 313–318 (2009)
18. T. Yuan, Z. Wei, J. Yuan, L. Yan, Q. Liu, J. Wang, *J. Sol-Gel Sci. Technol.* **58**, 501–506 (2011)
19. B. Ghosh, S. Kumar, *Hyperfine Interact.* **183**, 163–169 (2008)
20. V. Sreeja, S. Vijayanand, S. Deka, P.A. Joy, *Hyperfine Interact.* **183**, 99–107 (2008)
21. T. Prasada, M.C. Santhosh Kumar, S. Anbumozhi, M.Ashok Angayarkanni, *J. Alloys Compd.* **485**, 413–417 (2009)
22. S.S. Shinde, C.H. Bhosale, K.Y. Rajpure, *J. Mole Struct.* **1021**, 123–129 (2012)
23. A. Galal, O. Sadek, M. Soliman, S. Ebrahim, M. Anas, *Nat. Portf.* **11**, 20170 (2021)
24. J. Hwang, M. Choi, H.S. Shin, B.K. Ju, M. Chun, *Appl. Sci.* **10**, 6279 (2020)
25. T. Zhou, D. Zhang, L. Jia, F.B. Jin, Y. Liao, T. Wen, C. Liu, H. Su, N. Jia, Z. Zheng, V.G. Harris, H. Zhang, Z. Zhong, *J. Phys. Chem. C* **119**, 13207–13214 (2015)
26. X. Zhou, J. Wang, L. Zhou, D. Yao, *Appl. Phys. A* **128**, 306 (2022)
27. A. Takayama, M. Okuya, S. Kaneko, *Solid State Ionics* **172**, 257 (2004)
28. Z. Wu, M. Okuya, S. Kaneko, *Thin Solid Films* **385**, 109 (2001)
29. V.d. Pauw, *Philips Technique RDCH* **20**, 230 (1958)
30. V. d. Pauw, *Philips Res. Rept. Results* **13** 1 (1958)
31. A.E. Saba, E.M. Elsayed, M.M. Moharam, *J. Mater. Sci.* **46**, 3574–3582 (2011)
32. S. Bid, S.K. Pradhan, *J. Mater. Chem. Phys.* **84**, 291–301 (2004)
33. M. Saleem, L. Fang, H.B. Ruan, F. Wu, Q.L. Huang, C.L. Xu, C.Y. Kong, *Int. J. Phys. Sci.* **7**, 2971 (2012)
34. M. George, S.S. Nair, A.M. John, P.A. Joy, M.R. Anantharaman, *J. Phys. D* **39**, 900 (2006)
35. K. Kamala Bharathi, G. Markandeyulu, C.V. Ramana, *J. Phys. Chem. C* **115**, 554 (2011)
36. P. Scherrer, Bestimmung der Größe und der inneren Struktur von Kolloidteilchen mittels Röntgenstrahlen. *Nachr. Ges Wiss Göttingen* **26**, 98 (1918)
37. C.J. Rupp, S. Chakraborty, R. Ahuja, R.J. Baierle, *J. Mater. Chem. Phys.* **1**, 6 (2015)
38. A. Maher, W. Mohamed, B. Mohamed, *J. Magn. Magn. Mater.* **378**, 246–252 (2015)
39. S. Chakraverty, S. Mitra, K. Mandal, P.M.G. Nambissan, S. Chattopadhyay, *Ferrites* 136 (1959)
40. R. Sharma, S. Singhal, *Phys. B* **414**, 83–90 (2013)
41. C. Prakash, J.S. Baijal, *Solid State Commun.* **50**, 557 (1984)
42. M.B. Morales, M.H. Phan, S. Pal, N.A. Frey, *J. Appl. Phys.* **99** (2006)
43. F.W. Billmeyer Jr., P.J. Alessi, *Assessment of Color-Measuring Instruments*. Wiley, New York (1981)
44. D. R. Sahu, *J. Microchem.* **38** 1252 (2007)
45. R.Y. Krishnan, S. Manikandan, K.S. Suganthi, *J. Mater. Sci. Chemic Eng.* **699**, 524 (2001)
46. M. Oztas, M. Bedir, *Thin Solid Films* **516**, 1703 (2008)
47. A. Ayana, F. Hou, J. Seidel, B.V. Rajendra, P. Sharma, *Mater. Sci. Semiconduct. Process.* **146**, 106680 (2022)
48. D. Gao, Z. Shi, Y. Xu, J. Zhang, G. Yang, J. Zhang, X. Wang, D. Xue, *Nanoscale Res. Lett.* **5**, 1289 (2010)
49. A. Ayana, B. Neelamma, P.S. Gummagol, P. Patil, B.V.Rajendra Sharma, *Mater. Sci. Semiconduct. Process.* **133**, 105931 (2021)
50. R.J.D. Tilley et al., *Defects in Solids*. Wiley, New Jersey (2008)
51. Y. Reddy, B. Ajitha, P.S. Reddy, *Mater. Express* **4**, 32 (2014)
52. V. Jeseentharani, M. George, B. Jeyaraj, A. Dayalan, K.S. Nagaraja, *J. Exper. Nanosci.* **83**, 358–370 (2012)

Publisher's Note Springer Nature remains neutral with regard to jurisdictional claims in published maps and institutional affiliations.

Springer Nature or its licensor holds exclusive rights to this article under a publishing agreement with the author(s) or other rightsholder(s); author self-archiving of the accepted manuscript version of this article is solely governed by the terms of such publishing agreement and applicable law.